PAPER

Micro/nanostructured α-Fe₂O₃ spheres: synthesis, characterization, and structurally enhanced visible-light photocatalytic activity†

Gang Liu,[a] Quan Deng,[a] Hongqiang Wang,[a] Dickon H. L. Ng,[b] Mingguang Kong,[a] Weiping Cai[a] and Guozhong Wang*[a]

Micro/nanostructured α-Fe₂O₃ spheres (MNFSs) were fabricated *via* a surfactant- and template-free method, involving the hydrothermal synthesis of FeCO₃ precursor firstly and a subsequent thermal decomposition treatment. The product was characterized by X-ray diffraction, field emission scanning electron microscopy and transmission electron microscopy. The MNFSs had an average diameter of about 5 μm, and each contained subunits of interlinked and elongated particles with size less than 30 nm. The UV-Vis spectrum of MNFSs exhibited visible-light absorption. The visible-light photocatalytic activity of MNFSs was evaluated by using them to degrade the rhodamine 6G pollutant in water at ambient temperature under different parameters such as pH value, the amount of MNFSs and H₂O₂. We also found that the visible-light photocatalytic activity of MNFSs was higher than that of the micron- and nano-sized α-Fe₂O₃ particles. The reaction rate of MNFSs was more than twice that of nano-sized α-Fe₂O₃ and nearly 12 times faster than that of the micron-sized α-Fe₂O₃. This high photocatalytic feature of MNFSs was attributed to the high specific surface area together with their special porous structure. Importantly, these characteristics could control the rate of releasing ·OH and thus improve the utilization efficiency of ·OH. MNFSs can be easily recycled from the treated water using a magnet due to its magnetic behavior. There was no obvious decrease of the photocatalytic activity of MNFSs after being used.

1. Introduction

Semiconductor catalysts have been widely applied in heterogeneous photocatalysis for water disinfection, wastewater purification, and hazardous waste remediation.[1,2] Many efforts have been made to synthesize semiconductor photocatalysts with tunable sizes ranging from nano-size to micron-size and shapes to improve the photocatalytic activity.[3] As the size decreases to nano-size, semiconductors display more excellent catalytic activity resulting from their high specific surface area and high activity. However, one disadvantage of the nano-sized materials is the easy agglomeration due to their high surface energy, thus they would have reduced catalytic activity. In addition, the finely nano-sized catalysts could not be easily collected from the liquid system after use, resulting in low utilization and recontamination. Considering these shortcomings of nano-sized catalysts, more attention has been directed to the synthesis of micro/

nanostructured semiconductor catalysts.[2,4–7] They are micron-size, but are assembled from low-dimensional reactive nano-sized building blocks (such as nanoparticles, nanowires, nanotubes, and nanosheets). They have the merits of high dispersion and easy recovery of microstructures with the high activity and specific surface area of nanostructures. So far, a variety of micro/nanostructured materials have been fabricated and demonstrated enhanced catalytic performance.[2,4–10]

Hematite (α-Fe₂O₃) has a bandgap of 1.9 to 2.2 eV. It could be a potential semiconductor catalyst of visible-light driving.[4] Moreover, compared with other narrow bandgap semiconductors (CdS, WO₃, ZnIn₂S₄ and Bi₂WO₆),[7–10] α-Fe₂O₃ shows more excellent environmental compatibility, lower cost and high stability against photo-corrosion in aqueous solution.[11] In addition, it is easy to separate α-Fe₂O₃ powder from solution by magnet force. Due to these attractive characteristics, multifarious micro/nanostructured α-Fe₂O₃ have been fabricated by using self-assembly strategies[12–14] or organic/inorganic template methods (*e.g.* polystyrene sphere, carbon sphere, mesoporous silica), followed by thermal treatment or etching to remove the templates.[15–18] However, these synthetic processes are usually time consuming, and require extensive use of surfactants or tedious multi-step procedures. If α-Fe₂O₃ could be designed and synthesized in the form of micro/nanostructure, and their

[a]*Key Laboratory of Materials Physics, Anhui Key Laboratory of Nanomaterials and Nanotechnology, Institute of Solid State Physics, Chinese Academy of Sciences, P.O. Box 1129, Hefei 230031, P.R. China. E-mail: gzhwang@issp.ac.cn*
[b]*Department of Physics, The Chinese University of Hong Kong, Shatin, New Territory, Hong Kong*
† Electronic supplementary information (ESI) available. See DOI: 10.1039/c2jm31586f

9704 | *J. Mater. Chem.*, 2012, **22**, 9704–9713

This journal is © The Royal Society of Chemistry 2012

catalytic activity would be great enhancement and in favor of its application in liquid system. Therefore, a simple, cost-effective and eco-friendly method is preferred to synthesize micro/nano-structured α-Fe_2O_3 with high activity.

Herein, we demonstrated a practical and feasible method for synthesis of MNFSs by annealing micro/nanostructured $FeCO_3$ spheres after they were self-assembled into ultrathin nano-lamellar structures during a hydrothermal process. The $FeCO_3$ products were distinctly unlike the original $FeCO_3$ morphology such as solid faceted microparticles, microsphere, peanut-like or ellipsoidal microcrystals.[19–21] We have investigated the photo-catalytic ability of MNFSs under visible light for the degradation of rhodamine 6G (R6G). The results indicate that MNFSs exhibit structurally enhanced photocatalytic activity, compared with that using nano- or micron-sized α-Fe_2O_3 particles, due to its novel hierarchical porous structure and higher surface area. The photocatalytic influence parameters are also evaluated, such as the pH value, the amount of MNFSs and H_2O_2. The results reveal that the mainly reactive radical in the photocatalytic process is the hydroxyl radical ($\cdot OH$), which can be controlled and slow-released by MNFSs. MNFSs can improve the utilization efficiency of $\cdot OH$ and have good reproducibility in degradation of R6G.

2. Experimental section

2.1 Chemicals

All chemical reagents in our work were of analytical grade and used as received without further purification. Hexahydrated ferric chloride ($FeCl_3 \cdot 6H_2O$) (from Wuxi Zhanwang Chemical Co., Ltd, China), hydrogen peroxide (H_2O_2 30 wt%), urea ($CO(NH_2)_2$) (from Shanghai Suyi Regent Company, China) and ascorbic acid ($C_6H_8O_6$) (from Jinbei Fine Chemistry Regent Company, Tianjin, China), nanosized α-Fe_2O_3 (from Aladdin chemistry Co. Ltd) and micron-sized α-Fe_2O_3 (from Sinopharm Chemical Reagent Co. Ltd, China).

2.2 Synthesis of $FeCO_3$ and MNFSs

In a typical sample preparation procedure, 4 mmol of $FeCl_3 \cdot 6H_2O$, 4 mmol of $C_6H_8O_6$ and 10 mmol of $CO(NH_2)_2$ were dissolved into 40 mL deionized water under stirring to obtain a homogeneous solution. The mixture was transferred into a Teflon autoclave (70 mL) and was heated at 160 °C for 4 h in an electric oven. After cooling to room temperature, the precipitate was collected by centrifugation and was then washed with deionized water and ethanol before drying in a vacuum oven at 60 °C for 12 h. The product of $FeCO_3$ was obtained and it was further annealed at 500 °C for 4 h in air to obtain the MNFSs.

2.3 Characterization

The products were analyzed by X-ray diffraction (XRD) by using Cu-Kα radiation (Philips X'pert diffractometer). The surface area of the products was determined by nitrogen adsorption at 77 K (Micrometrics ASAP 2020M). The morphology of the prepared products was studied by field emission scanning electron microscopy (FESEM, Sirion 200 FEI) and transmission electron microscopy (TEM, JEOL-2010,

200 kV) with an energy-dispersive X-ray spectrometer (EDS, Oxford, Link ISIS). The samples for microscopy studies were prepared by deposition of dispersions of the powder in ethanol directly on the FESEM stubs or holey carbon grid for TEM examination. UV-visible diffused reflectance spectra of α-Fe_2O_3 powder were obtained for the dry-pressed disk samples using a UV-visible spectrophotometer (UV-3600, Shimadzu, Japan). $BaSO_4$ was used as a reflectance standard in a UV-visible diffuse reflectance experiment. Magnetic measurement was performed with a superconducting quantum interference device (SQUID) magnetometer (Quantum Design, MPMS XL).

2.4 Measurement of photocatalytic activity

The photocatalytic activity of the as-prepared samples was evaluated by photocatalytic degradation of R6G pollutants at ambient temperature. The experimental procedures were performed as follows. 40 mg of the as-prepared MNFSs powder was dispersed in 1.25×10^{-5} mol L^{-1} R6G aqueous solution (40 mL, pH 6.5) in a cylinder-shaped cell (diameter 60 mm × height 60 mm), followed by the addition of 0.3 mL of H_2O_2 solution (30 wt%). The above solution was irradiated in a biological incubator (MLR-351H, SANYO, fluorescent lamp 40 W with the wavelength of 400–700 nm) under continuous stirring (experimental environments were set under 5LS irradiation visible light (1LS = 5 fluorescent lamps) at 25 °C constant temperature). Before visible-light irradiation, the solution was stirred for 30 min in the dark to reach an adsorption–desorption equilibrium among the MNFSs, R6G and H_2O_2. Analytical samples (1.5 mL) for absorption measurement were taken out from the reaction suspension at different time intervals, centrifuged at 7000 rpm for 2 min to remove the catalyst of MNFSs. A spectrophotometer (CARY-5E) was used to record UV-Vis absorption spectra of the centrifuged solutions.

The durability of the photocatalytic activity of the as-prepared MNFSs was also studied by re-using the catalysts under the visible-light irradiation, which was performed at the same ratio of the as-prepared MNFSs to R6G. For the first cycle, 1.5 mL mixture solution of R6G and the catalyst was taken out as the test sample after the photocatalysis performed for 30 and 60 min, respectively. After the first cycle, all of the solutions, including the taken-out samples, were brought back to centrifuge, washed and distilled, then the obtained powder was re-used for the second time. The processes of the second and following cycles were as above.

Photocatalytic influence parameters such as the amount of H_2O_2 (0, 50, 100, 300, 700, 1000 μL), MNFSs (0, 0.25, 0.5, 1, 1.5, 2 g L^{-1}), and pH value (2, 3, 6.5, 9, 11) were also studied, and the experimental procedures were similar to the measurement of photocatalytic activity. Further comparative experiment of 40 mg micron-sized α-Fe_2O_3 (diameter about 3–5 μm and specific surface area 2.91 m^2 g^{-1}) and nano-sized α-Fe_2O_3 (with average diameter about 30 nm and specific surface area 9.86 m^2 g^{-1}), as shown in Fig. S1† were also carried out to investigate the photocatalytic activity.

The effects of photogenerated holes on the photocatalytic process using MNFSs was evaluated by using methanol (CH_3OH) as a hole scavenger.[22] The experimental procedures were similar to the measurement of photocatalytic activity except

This journal is © The Royal Society of Chemistry 2012

J. Mater. Chem., 2012, **22**, 9704–9713 | 9705

that a mixture of R6G aqueous solution with 1 mol L^{-1} CH$_3$OH was used.

Photocatalytic degradation efficiency (D%) of the products could be determined by detecting the intensity of absorption peak (at 526 nm) of the treated R6G solution under irradiation. The D value can be calculated by the following equation:[23]

$$D\% = \left[\frac{C_0 - C}{C_0}\right] \times 100\% \qquad (1)$$

where C_0 is the initial concentration of R6G, and C is the reaction or balance concentration of R6G after irradiation in a selected time interval.

2.5 Analysis of ·OH

To confirm the presence of the ·OH groups, the photoluminescence (PL) technique was employed. It utilized terephthalic acid as a probe molecule as previously reported.[24] Experimental procedures were similar to the measurement of photocatalytic activity except that the mixed solution of 3 mmol L^{-1} terephthalic acid with a concentration of 0.01 mol L^{-1} NaOH was being used. The PL spectra of generated 2-hydroxyterephthalic acid were carried out on a FluoroMax-4 fluorescence spectrometer (Horiba Jobin Yvon Inc., France). After being irradiated by a 320 nm light at 25 °C for different durations, each reaction solution was filtrated to measure the change in PL intensity of the 425 nm peak. The excitation and emission slits were all set at 1 nm for all the fluorescent measurements.

Electron spin resonance (ESR) experiments were also performed at room temperature on the JES-FA200 (JEOL) equipped with an *in situ* irradiation source (500 W Xe lamp). The same quartz capillary tube was used in all these measurements. In the ESR measurement, the following parameters were adopted. The microwave frequency was 9073 MHz, and its power was 1 mW. The modulation frequency was 100 kHz. The solution of 5,5-dimethyl-1-pyrroline-*N*-oxide (DMPO) was used as the spin trap for ·OH.[25]

3. Results and discussion

3.1 Structure and morphology of the products

XRD was used to investigate the phase structure of the products. The diffraction peaks of the precursor can be indexed to rhombohedral phase (space group: $R\bar{3}c$ (167)) of FeCO$_3$ (JCPDS card No: 29-0696), as shown in Fig. 1a. To obtain more information of the structure before annealing, the sample was characterized by electron microscopy. Fig. 1b is a typical FESEM image of the micro/nanostructured FeCO$_3$ spheres, in which large quantities of monodisperse hierarchical sphere-like structure could be observed. Their diameter was estimated to be about 500 to 5000 nm. The high-magnified SEM image (Fig. 1c) revealed that these FeCO$_3$ spheres were composed of numerous ultra-thin nano-lamella structures and they were inter-connected. In the corresponding high resolution TEM image, it was clearly seen that the average thickness of these lamella unit was about 6.5 nm, as indicated by the arrows in Fig. 1d. The EDS analysis was also employed to study the composition of the micro/nanostructured FeCO$_3$ spheres. As shown in the insert of Fig. 1d, the as-synthesized products were composed of Fe, O, C, and Cu
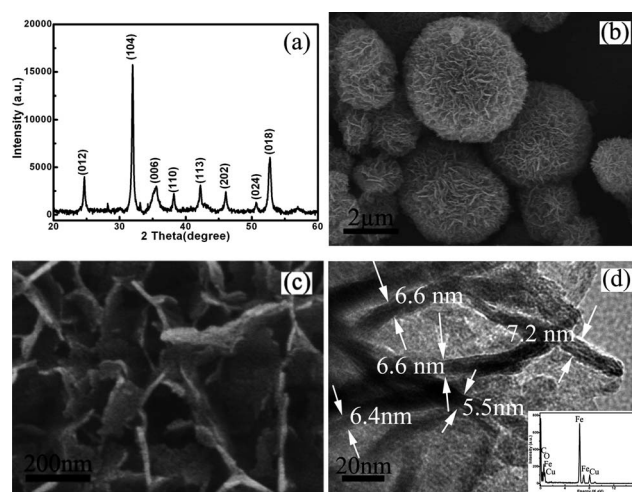

Fig. 1 Structural characterization of the as-prepared FeCO$_3$ spheres: (a) XRD pattern, (b) and (c) are the low and high magnification FESEM images, respectively. (d) TEM images of the surface of FeCO$_3$ spheres and the insert is the EDX pattern.

elements. Among them, C, Fe and O signals were originated from the FeCO$_3$ crystals. Some of the C would belong to the carbon film, and Cu was from the copper grid.

Ascorbic acid (AA) has an significantly effect on the formation of the spherical FeCO$_3$. Fig. 2 shows FESEM images of the products at different amount of AA and their corresponding XRD patterns. In the absence of AA (as shown in Fig. 2a), only α-Fe$_2$O$_3$ pseudocubic particles were formed as follows (eqn (2) and (3)) :

$$Fe^{3+} + 3OH^- \rightarrow Fe(OH)_3 \qquad (2)$$

$$2Fe(OH)_3 \rightarrow Fe_2O_3 + 3H_2O \qquad (3)$$

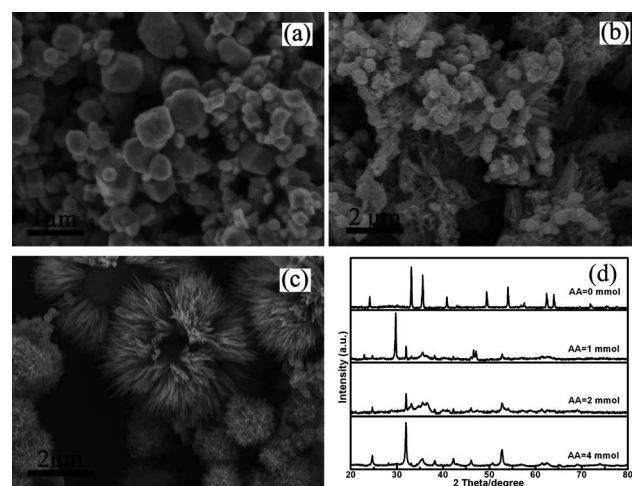$$2Fe^{3+} + C_6H_8O_6 \rightarrow 2Fe^{2+} + C_6H_6O_6 + 2H^+ \qquad (4)$$
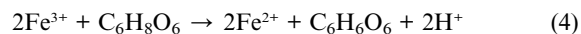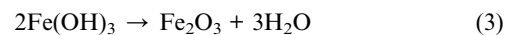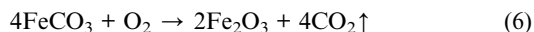

Fig. 2 FESEM images of the products obtained by the hydrothermal method with different amount of AA heated at 160 °C for 4 h: (a) 0 mmol, (b) 1 mmol, (c) 2 mmol. (d) The XRD patterns of the corresponding products.

$$Fe^{2+} + 2OH^- + CO_2 \rightarrow FeCO_3 + H_2O \qquad (5)$$

$$4FeCO_3 + O_2 \rightarrow 2Fe_2O_3 + 4CO_2\uparrow \qquad (6)$$

When the AA was presented, Fe^{3+} could be reduced as in eqn (4),[20] then the $FeCO_3$ was formed as eqn (5). As the amount of AA increased from 1 mmol to 4 mmol, the morphology of the as-prepared product changed from irregular particles (Fig. 2b) to the regular three dimensions spherical $FeCO_3$ (Fig. 1b). And the corresponding XRD patterns (Fig. 2d) indicated that the main peak of $FeCO_3$ located at 2θ values of 31.99° increased obviously with the increasing amount of AA. When the amount of AA was up to 4 mmol, perfectly spherical $FeCO_3$ was formed.

We know that the growth behavior of crystals is mainly determined by the internal structure of a given crystal. The carbonate ions (CO_3^{2-}) have planar structure and the bond angle of O–C–O is 120°. This structure is of compatible with the observed symmetry of the ion, and the three bonds are equally long and the three oxygen atoms are equivalent. When Fe^{2+} and CO_3^{2-} combined to form $FeCO_3$ crystal nuclei, the iron and oxygen atoms tended to form Fe–O octahedron between the different planes of CO_3^{2-}. As a result, the generated $FeCO_3$ tended to grow in lamellar structure and finally the nanosized lamellar structure self-assembled into $FeCO_3$ micro-spheres through oriented attachment mechanism during the hydrothermal process.[13] Finally, the MNFSs were obtained by annealing the $FeCO_3$ spheres in air as the eqn (6).[20] The releasing of CO_2 in the lamellar structure resulted in the formation of porous micro/nanostructured α-Fe_2O_3 spheres.

Fig. 3a shows the XRD pattern of the MNFSs after annealing the precursor $FeCO_3$ at 500 °C for 4 h in air. All the diffraction peaks could be indexed to the rhombohedral phase (space group: $R\bar{3}c$ (167)) of α-Fe_2O_3 (JCPDS card No: 33-0664). After the precursor $FeCO_3$ micro-spheres were annealed at 500 °C for 4 h in air, the lamellar structure was transformed to inter-leaved nanoparticles, leading to the formation of MNFSs as shown in Fig. 3b and 3d. However, the size of MNFSs (Fig. 3b and 3d) was unchanged same as the original $FeCO_3$ micro-sphere precursor with the diameter of about 500 to 5000 nm. The lamellar structure was transformed to inter-linked and elongated particles with a diameter of about 5 to 30 nm (Fig. 3c and S2). The TEM image (Fig. 3d and S2) revealed that the MNFSs had a porous structure. From the TEM image in Fig. 3e, the fringe of the particle in a MNFSs corresponded to an interplanar distance of 0.252 nm. This agreed well with the lattice spacing of the (110) plane of α-Fe_2O_3.

Nitrogen adsorption/desorption isotherms were measured to determine the specific surface area and pore size distribution of the MNFSs product. The results are presented in Fig. 3f. According to Brunauer–Deming–Deming–Teller classification,[26] the sample exhibited a type H1 hysteresis loop, indicating the presence of mesopores (2–50 nm). The observed hysteresis loops shifted to a high relative pressure $P/P_0 \approx 1$, suggesting the presence of large pores (>50 nm). From the pore size distribution of MNFSs (insert in Fig. 3f), derived from desorption data, we found that the pore size distribution was not uniform, and the pore sizes were distributed around 2 and 50 nm. This result was consistent with the results of our previous TEM analysis (see
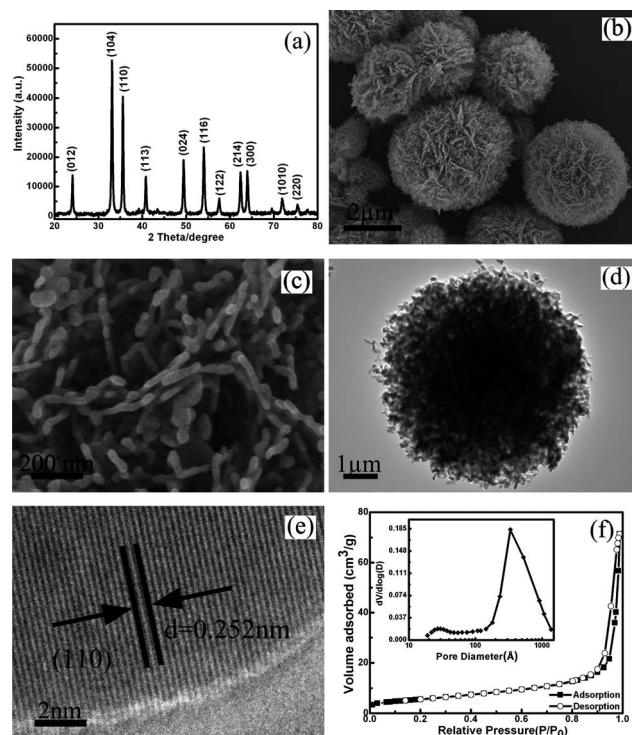

Fig. 3 Structural characterization of the as-prepared MNFSs obtained by annealing the precursor of $FeCO_3$ spheres at 500 °C for 4 h in air: (a) XRD pattern, (b) and (c) are low and high magnification FESEM images of MNFSs, respectively. (d) TEM image of single MNFSs. (e) HRTEM image of the MNFSs particles. (f) Nitrogen adsorption/desorption isotherms and pore size distribution curve (insert) of MNFSs powder.

Fig. S2†). The pore volume of MNFSs was 0.11 $cm^3\ g^{-1}$, and the specific surface area MNFSs was found to be 20 $m^2\ g^{-1}$ based on the results from N_2 adsorption. Our results were overall larger than that of α-Fe_2O_3 reported by others when they were in the forms of hollow spindles (16.55 $m^2\ g^{-1}$), micro-spheres (13.07 $m^2\ g^{-1}$) and cantaloupe-like superstructures (9.82 $m^2\ g^{-1}$).[27,28]

We had also measured the magnetic hysteresis of MNFSs at room temperature (Fig. S3†). In the measurement, the applied field was swept between −45 and 45 kOe. The product exhibited hysteresis in the low field regime, suggesting that MNFSs exhibit ferromagnetic behaviors at room temperature, which is similar to the reported cases in the literature.[4,12,13,18,28] The remnant magnetization (M_r) and coercivity (H_c) were found at 0.67 emu g^{-1} and 65 Oe, respectively. Owing to their ferromagnetic behaviors, MNFSs could be easily separated and collected through the magnetic separation process.

3.2 Optical properties and photocatalytic activity

The optical absorption properties could reveal the spectrum range that light is being absorbed to excite the electrons in a catalyst.[29] The optical absorption of the MNFSs product was investigated by using UV-Vis spectroscopy at room temperature (Fig. 4a). It showed an obvious absorption at the wavelengths shorter than 600 nm, indicating that MNFSs could function under the visible light. We also found that the products had an obvious blue-shift in the bandgap transition as its crystallite size
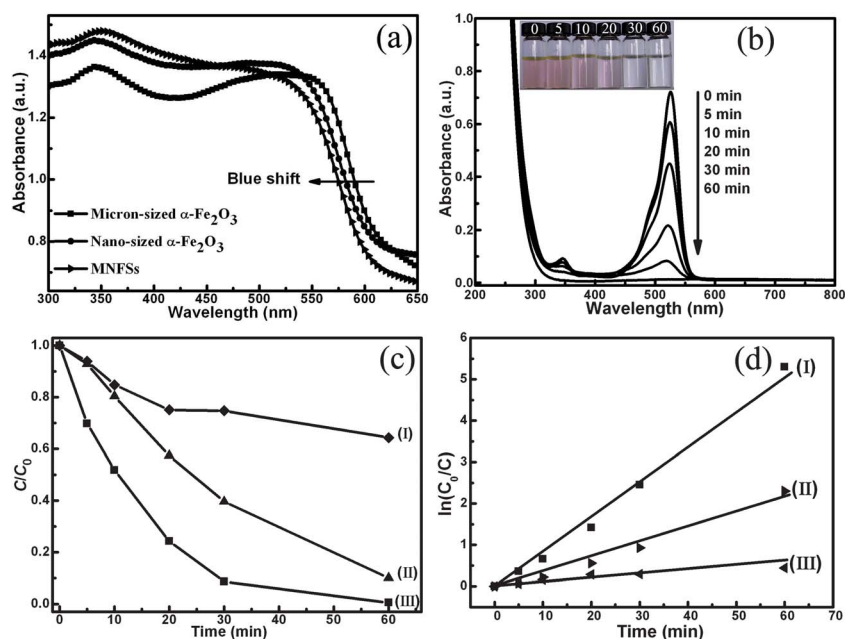
This journal is © The Royal Society of Chemistry 2012

J. Mater. Chem., 2012, **22**, 9704–9713 | 9707

Fig. 4 (a) The UV-Vis spectra for nano- and micron-sized α-Fe$_2$O$_3$, and MNFSs samples. (b) Changes of time-dependent UV-Vis absorbance spectra in the presence of MNFSs with H$_2$O$_2$ under visible-light irradiation for different times and (insert) photographs of the corresponding color change of R6G solutions. (c) Photodegradation of R6G by different catalysts with H$_2$O$_2$ under the visible-light irradiation for 60 min: (I) micron-sized α-Fe$_2$O$_3$ particles; (II) nano-sized α-Fe$_2$O$_3$ particles and (III) MNFSs. (d) Kinetic study of the degradation of R6G by MNFSs (I); nano-sized α-Fe$_2$O$_3$ (II) and micron-sized α-Fe$_2$O$_3$ (III). C and C_0 denote the reaction and initial concentration of R6G in the system, respectively.

decreased. The blue-shift of the MNFSs was much larger than those of the nano- and micron-sized α-Fe$_2$O$_3$ particles. The possible reason was that the size of the crystallites (a diameter of about 5 to 30 nm) in the MNFSs was smaller than those of nano-sized α-Fe$_2$O$_3$ (with average diameter about 30 nm) and micron-sized α-Fe$_2$O$_3$.

The visible-light photocatalytic activity of MNFSs was evaluated by using it to degrade the R6G dye aqueous solution in the presence of H$_2$O$_2$. The photocatalytic degradation process was monitored through the change in intensity of the characteristic absorption peak of R6G at 526 nm. The absorption spectrum of R6G solution showed time-dependent change in the presence of MNFSs under visible-light irradiation as shown in Fig. 4b. The characteristic absorption peak of R6G molecules at 526 nm rapidly decreased in intensity as time prolonged and it disappeared completely after about 60 min. The insert (top) of Fig. 4b showed a series of color changes corresponding to the sequential change of the R6G solution with the MNFSs powder after being exposed to the visible light for different time durations. It was evident that the color of the solution gradually changed from intense pink to colorless as the exposure time increased. The comparative photocatalytic results of MNFSs, nano- and micron-sized α-Fe$_2$O$_3$ spheres are shown in Fig. 4c. It indicated that the degradation rate of R6G by MNFSs was much faster than those of the nano- and micron-sized α-Fe$_2$O$_3$ at the same exposure time. After 60 min irradiation, most of the R6G was decomposed in solution with MNFSs, while 10% and 64% of R6G still remained in those with the nano- and micron-sized α-Fe$_2$O$_3$, respectively.

The photocatalysts degradation kinetic reaction can be described by a modified Langmuir–Hinshelwood model.[23,30] The

apparent rate constant (k_{app}) is the basic kinetic parameter for the different photocatalysts, reflecting the reaction rate of a photocatalytic process. The apparent first order kinetic eqn (7) is used to fit experimental data from the Fig. 4c:

$$\ln\left(\frac{C_0}{C}\right) = k_{app}t \tag{7}$$

where C is the concentration of solute remaining in the solution after irradiation time t, and C_0 is the initial concentration at $t = 0$. The variations in $\ln(C_0/C)$ as a function of irradiation time is given in Fig. 4d. The calculated data for k_{app} for MNFSs, micron- and nano-sized α-Fe$_2$O$_3$ are listed in Table 1. We found that the value of k_{app} of MNFSs was twice that of the nano-sized α-Fe$_2$O$_3$ and nearly 12 times larger than that of the micron-sized α-Fe$_2$O$_3$, indicating that the k_{app} was enhanced by using α-Fe$_2$O$_3$ in the form of a micro-sphere with nano-sized crystallites.

3.3 The amount of H$_2$O$_2$, MNFSs and the pH value effect on the photocatalytic efficiency

The effect of H$_2$O$_2$ amount on the degradation of R6G was investigated and the result was depicted in Fig. 5a. The result

Table 1 Apparent rate constant data for different samples

| Samples	MNFSs	Nano-sized α-Fe$_2$O$_3$	Micron-sized α-Fe$_2$O$_3$
BET/m^2 g^{-1}	20	9.8	2.9
K_{app}/min^{-1}	0.0892	0.0391	0.007
R^2	0.9938	0.9836	0.8579
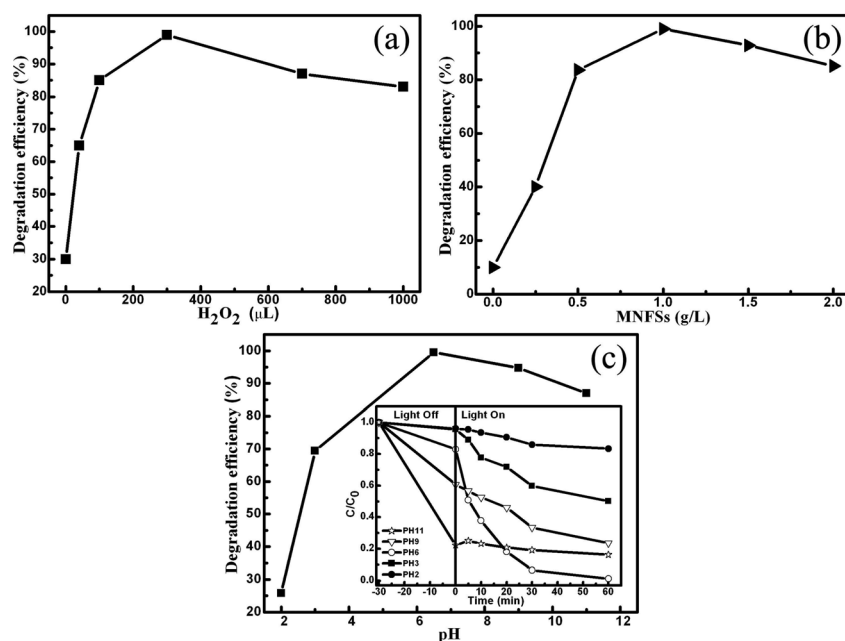
Fig. 5 Effect of the reaction parameters on the photodegradation of R6G under the visible-light irradiation for 60 min by (a) H_2O_2, (b) MNFSs and (c) the initial pH value and (insert) the photocatalytic degradation of R6G by MNFSs with the time evolution under the different pH value.

showed that the photocatalytic degradation efficiency of R6G increased first, and decreased as the H_2O_2 amount increased. The degradation efficiency reached the maximum under the amount of H_2O_2 around 300 μL, then it decreased slightly above and below this value. With the H_2O_2 amount increasing from 0 to 300 μL, the photocatalytic degradation efficiency of R6G increased to nearly 100% after 60 min irradiation. It was possible that more radicals were formed with increasing H_2O_2, thus leading to an increase of the reaction rate.[31] However, when the amount of H_2O_2 further increased from 300 to 1000 μL, the rate of degradation of R6G decreased to a certain extent. Excess H_2O_2 would result in a self-consumption and scavenging effect of ·OH through the reaction described by eqn (8) and (9).[25,32,33]

$$H_2O_2 + \cdot OH \rightarrow \cdot HO_2 + H_2O \quad (8)$$

$$\cdot HO_2 + \cdot OH \rightarrow O_2 + H_2O \quad (9)$$
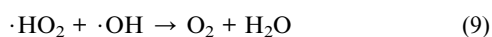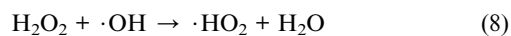
The effect of the MNFSs amount on photocatalytic degradation efficiency has been studied, and the result is shown in Fig. 5b. As the amount of photocatalyst increased, the degradation efficiency of R6G firstly increased and then decreased. It finally reached the maximum removal efficiency when the amount of MNFSs was 1 g L^{-1}. As the amount of MNFSs increased from 0 to 1 g L^{-1}, it could effectively increase the amount of active sites to produce more ·OH, thereby accelerating the degradation efficiency of R6G.[31] However, excessive addition of MNFSs beyond 1 to 2 g L^{-1} would result in a weaken effect on the degradation efficiency. There might be two primary reasons for the decrease: (i) over supply of MNFSs increased the amount of ·OH, caused the scavenging according to eqn (8) and (9); (ii) the shielding effect, caused by superfluous MNFSs, prevented the penetration of light and limited light adsorption on the surface of MNFSs.[34,35]

The influence of pH value on the photodegradation of R6G was also investigated by varying pH from 2 to 11 through the addition of HCl or NaOH. The influence effect of pH value had the similar tendency as the above results of H_2O_2 and MNFSs. From the Fig. 5c, the photodegradation efficiency of R6G increased firstly and then decreased with the pH value changing from 2 to 11, *i.e.* the maximum degradation efficiency was about 100% at pH 6.5. From the insert of Fig. 5c, we could see that the pH value strongly affected the adsorption of R6G onto the MNFSs surface under the dark conditions (light off) and the photocatalytic degradation efficiency of R6G under visible-light irradiation (light on). For the MNFSs has the amphoteric character with a point zero charge around pH 6.7.[36] At the same time, the R6G is the cation compound. As the surface charge of MNFSs changed from positive to negative with the pH value increasing from 2 to 11, this led to the enhancement of the R6G adsorbed onto MNFSs. It could be seen clearly under the light off conditions, which would strengthen the contact reaction of MNFSs and R6G. The reason for the degradation efficiency of R6G is that, under acidic conditions, H$^+$ has a scavenging effect on ·OH as in eqn (10),[37] thus, increasing the pH from 2 to 6.5 can reduce the scavenging effect by decreasing H$^+$ concentration, which efficiently increases the amount of active ·OH and enhances the photocatalytic efficiency. Finally, the photocatalytic degradation efficiency of R6G decreased with the pH increasing from 6.5 to 11, which mainly H_2O_2 could be decomposed to H_2O and O_2 under alkaline conditions following eqn (11),[38] and the increasing of pH (from 6.5 to 11) can reduce the oxidation potential of ·OH radical.[39]

$$H^+ + \cdot OH + e^- \rightarrow H_2O \quad (10)$$

$$2H_2O_2 \rightarrow 2H_2O + O_2\uparrow \quad (11)$$
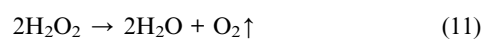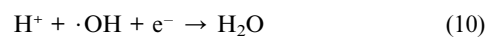
3.4 Photostability of MNFSs

The photostability of MNFSs was evaluated by re-using the catalysts in a fresh R6G solution under visible-light irradiation. The detailed experimental process was similar to that previously reported.[40] Fig. 6a shows the recycled experiments of the photodegradation of R6G for six cycles (60 min irradiation for each cycle). It was observed that 100% of R6G was photodegraded when MNFS photocatalyst was used for the first time. After six successive cycles, 90% of R6G was photodegraded, the photocatalytic activity of MNFSs photocatalyst almost remained unchanged, indicating that MNFSs photocatalyst was photostable during the photodegradation of R6G. In our work, a special advantage of using MNFSs to handle pollutants was that it would be easily separated and collected by an external magnet (shown in Fig. 6b and 6c), which was much easier than the centrifugal separation of non-magnetic ZnO or TiO$_2$ nanoparticles from the solution.

3.5 Photocatalytic mechanism

It is well known that the ·OH plays a key role in the photocatalytic reaction of α-Fe$_2$O$_3$ and H$_2$O$_2$.[4,22] The generated ·OH exists for a short-lived time (10^{-9} s),[41] and is generally annihilated before it reacts with pollutants. Not all ·OH are formed and have high effective efficiency. In the photocatalytic reaction, it is important to control the slow-release of ·OH and improve the efficiency of using ·OH and avoid the annihilation phenomenon. In our work, we present a feasible method to enhance the efficiency in the use of ·OH by the micro/nanostructured materials.

To confirm the reactive radicals involved in the photocatalytic reaction, the ESR spin-trap technique was employed to detect the reactive species generated from the mixed solution of MNFSs and H$_2$O$_2$ under visible-light irradiation. As shown in Fig. 7a, the ESR spectrum displayed a 4-fold characteristic peak of the typical DMPO-·OH adduct with a peak intensity ratio of 1 : 2 : 2 : 1 under visible-light irradiation,[25] which indicated that ·OH indeed existed in the photocatalytic degradation reaction of R6G and MNFSs with H$_2$O$_2$ under visible-light irradiation.

In order to understand the mechanism of the release of ·OH controlled by MNFSs, experiments were carried out as follows. The formation of ·OH under visible-light irradiation could be also detected by the PL technique using terephthalic acid as a probe molecule as it would readily react with ·OH to produce highly fluorescent product 2-hydroxyterephthalic acid.[24] The PL intensity of the 2-hydroxyterephtalic acid at 425 nm is proportional to the amount of ·OH produced on the surface of the photocatalyst. Fig. 7b shows the fluorescence spectra of the aqueous basic solution of terephthalic acid with excitation at 320 nm under different conditions. As shown in curve I of Fig. 7b, in striking contrast to TiO$_2$ or ZnO,[42] MNFSs without H$_2$O$_2$ under visible-light irradiation for 60 min, no
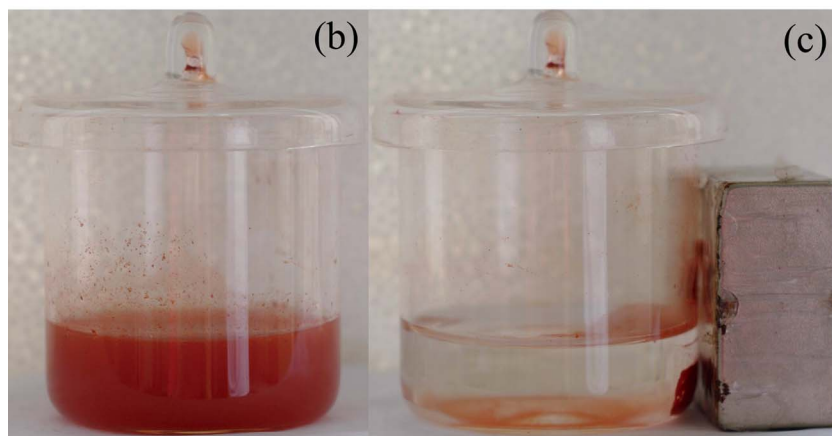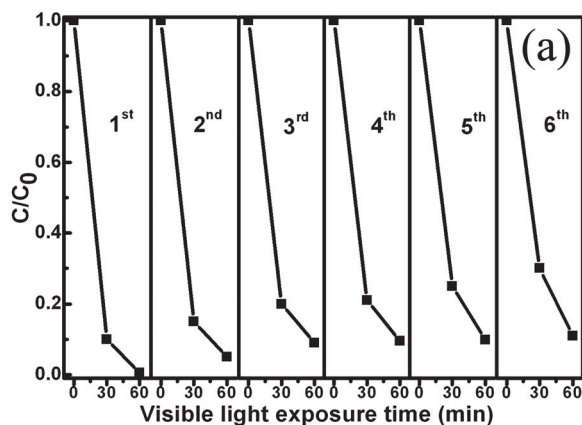

Fig. 6 (a) Photodegradation performance of MNFSs toward 1.25×10^{-5} mol L^{-1} R6G solutions within six cycles under visible-light irradiation. Photographs of the R6G solutions for photocatalytic degradation before (b) and after magnetic separation (c).
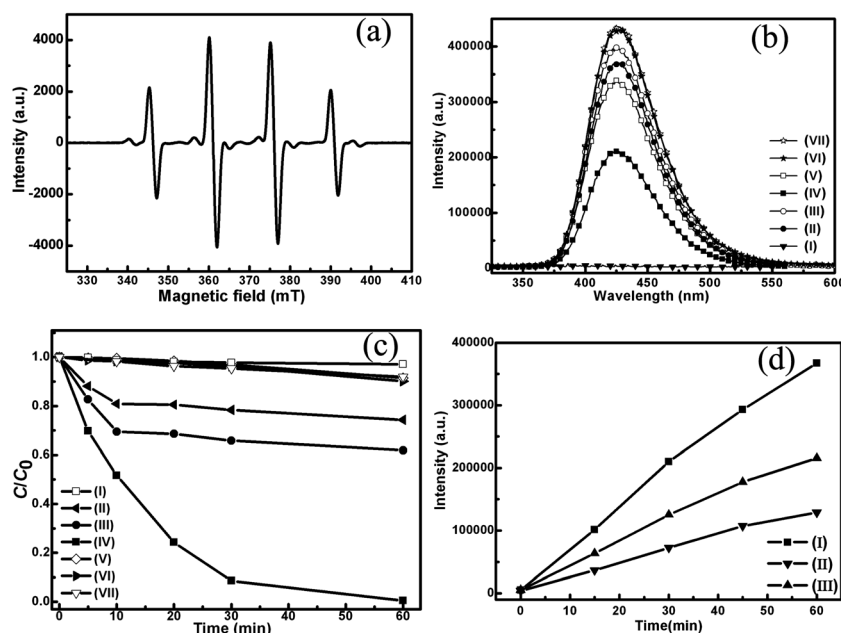
Fig. 7 (a) DMPO spin-trapping ESR spectra of a MNFS/H$_2$O$_2$/R6G/water suspension under Xe lamp (500 W) irradiation. (b) PL spectral of the aqueous basic solution of terephthalic acid under visible-light irradiation for different conditions: (I) MNFSs illuminated for 60 min; (II) MNFSs–H$_2$O$_2$ illuminated for 60 min; (III) H$_2$O$_2$ illuminated for 60 min; (IV) MNFSs–H$_2$O$_2$ illuminated for 30 min; (V) H$_2$O$_2$ illuminated for 30 min; (VI) MNFSs–H$_2$O$_2$ illuminated for 120 min and (VII) H$_2$O$_2$ illuminated for 120 min. (c) Photodegradation of R6G illuminated for 60 min under different conditions, depicted by the intensity decrease of R6G absorption peak at 526 nm: (I) R6G dye under visible-light irradiation without any MNFSs and H$_2$O$_2$; (II) H$_2$O$_2$ under visible-light irradiation without MNFSs; (III) MNFSs under visible-light irradiation without H$_2$O$_2$; (IV) MNFSs and H$_2$O$_2$ under visible-light irradiation; (V) MNFSs and CH$_3$OH under visible-light irradiation; (VI) MNFSs and H$_2$O$_2$ without visible-light irradiation and (VII) MNFSs and R6G without H$_2$O$_2$ in dark conditions. (d) PL spectral intensity changes of different α-Fe$_2$O$_3$ catalysts with H$_2$O$_2$ *versus* exposure time for 60 min under visible-light irradiation: (I) MNFSs; (II) nano-sized α-Fe$_2$O$_3$ and (III) micron-sized α-Fe$_2$O$_3$.

detectable ·OH was probed by the PL technique. Relative to the case without H$_2$O$_2$, MNFSs with H$_2$O$_2$ addition under the visible-light irradiation for 60 min, resulted in a strong PL peak around 425 nm (curve II). This demonstrated that a large amount of ·OH was formed in the presence of H$_2$O$_2$ and MNFSs under visible-light irradiation. However, in the absence of MNFSs under the visible-light irradiation for 60 min, the H$_2$O$_2$ solution exhibited a stronger PL peak around 425 nm (curve III) than that of MNFSs with H$_2$O$_2$ solution. A similar phenomenon was observed under visible-light irradiation for 30 min, seen from curves IV and V. However, when the time of visible-light irradiation was prolonged to 120 min, the PL intensity of MNFSs with H$_2$O$_2$ solution was the same as that of H$_2$O$_2$ solution, seen from curves VI and VII. It indicated that the same amount of ·OH was formed in the presence of H$_2$O$_2$ or MNFSs with H$_2$O$_2$ under visible-light irradiation for long enough exposure time, and the generation rate of ·OH from H$_2$O$_2$ was much faster than that of MNFSs with H$_2$O$_2$. These results were attributed to the slow-release of ·OH from H$_2$O$_2$ controlled by MNFSs.

Fig. 7c shows the results of the photocatalytic degradation of R6G with different conditions under visible-light irradiation for 60 min. Initially, blank experiments indicated that the photodegradation of R6G was negligible under visible-light irradiation without addition of any catalyst and H$_2$O$_2$ (curve I). Under visible-light irradiation without MNFSs, H$_2$O$_2$ exhibited a weak activity for the degrading R6G, and the degradation efficiency only reached 26% (curve II). In the absence of H$_2$O$_2$, MNFSs

showed weak photocatalytic activity under visible-light irradiation, and the degradation efficiency of R6G reached 38% (curve III). However, MNFSs showed an obviously visible-light photocatalytic activity in the presence of H$_2$O$_2$ under visible-light irradiation (curve IV), and the degradation efficiency could reach nearly 100%.

From curves II and III in Fig. 7b, about the same amount of ·OH was formed from H$_2$O$_2$ in the absence or presence of MNFSs under the visible-light irradiation for 60 min, but the degradation efficiency of R6G reached 26% or 100%, respectively (seen from curves II and IV of Fig. 7c). This confirmed that the use efficiency of ·OH was improved by the MNFSs, and most ·OH annihilated soon before it reacted with R6G in the reaction system without MNFSs. However, in the presence of MNFSs, the ·OH generated from H$_2$O$_2$ would be controlled by MNFSs, and the slow-release of ·OH prevented the interaction of ·OH and H$_2$O$_2$ followed as eqn (8) and (9), further improved the use efficiency of ·OH and avoided the annihilation phenomenon.

However, the degradation efficiency of R6G by MNFSs could reach 38% (curve III of Fig. 7c), which was attributed to the photogenerated holes formed on the MNFSs photocatalyst, as confirmed by using CH$_3$OH as a hole scavenger in the photodegradation of R6G.[22,43,44] The addition of excess CH$_3$OH (1 mol L^{-1}) led to the decrease of the degradation efficiency of R6G in the absence of H$_2$O$_2$ changed from 38% (curve III) to 10% (curve V). The aqueous solution of R6G and MNFSs was stirred in the dark without H$_2$O$_2$ for 60 min to reach the adsorption

equilibrium of R6G with the catalyst. The maximum adsorption capacity of MNFSs for R6G was about 8% (curve VII). It showed that the photogenerated holes were formed, and could affect the photodegradation of R6G. These results indicate that the photocatalytic activity of R6G was significantly improved with the cooperation of MNFSs and H_2O_2 compared to the individual MNFSs or H_2O_2.

We also investigated the PL intensity of the different morphologies of α-Fe_2O_3 catalyst under the visible-light irradiation for different durations. Compared with the PL intensity of nano- and micron-sized α-Fe_2O_3 (Fig. 7d), MNFSs clearly showed more ·OH releasing from H_2O_2 under the visible-light irradiation for the same time. It indicated that MNFSs had the structure enhanced catalytic activity for degradation of R6G under the same condition, which mainly attributed to MNFSs' high specific surface area together with the special porous structure (porosity about 57%). MNFSs were not only responsible to the slow-release of ·OH from H_2O_2 and improved the efficiency in the use of ·OH to avoid the annihilation phenomenon, but also their large surface area enhanced the adsorption of R6G on the surface of MNFSs.

Additionally, an experiment was also performed in the presence of MNFSs with H_2O_2 without visible-light irradiation (curve VI of Fig. 7c). It should be noted that the maximum adsorption capacity of MNFSs was about 10% decrease of R6G concentration. The interconnected pores of MNFSs (pore volume 0.11 cm^3 g^{-1}) enable storage of more H_2O_2 and contaminant molecules. Therefore, there are also two unique virtues of pores in MNFSs to enhance visible-light photocatalytic performance: (i) The feature of a hierarchical porous superstructure provides ideal channels for easy and fast diffusion of the R6G molecules into the internal surface of MNFSs, which greatly increases the collision probability between active radicals and R6G molecules, and leads to a higher degradation efficiency than other nano- and micron-sized samples. (ii) The nanoholes have bi-pore-size-distribution in MNFSs (see the insert of Fig. 3f), the bigger pore-size nanoholes along the radial are transparent for visible-light, which greatly increases the utilizing efficiency of visible-light, allowing multiple reflections of visible light within the interior that facilitates more efficient use of the light source and enhances light-harvesting, leading to an increased quantity of more ·OH available to participate in the photocatalytic degradation of R6G.[40,45,46] Therefore, the above results indicate that the degradation of R6G aqueous solution was mainly caused by photocatalytic degradation reaction instead of adsorption on the porous MNFSs under visible-light irradiation, and MNFSs showed structure enhanced visible-light photocatalytic activity.

4. Conclusions

Large scaled MNFSs had been fabricated using micro/nano-scaled $FeCO_3$ spheres as the precursor obtained by a controlled ascorbic-acid-assisted hydrothermal process, and subsequent annealing at 500 °C for 4 h in air. The as-prepared MNFSs exhibited superior photocatalytic activity in the photocatalytic degradation of R6G aqueous solution under visible-light irradiation. Under the optimized conditions (i.e. MNFSs 1g L^{-1}, H_2O_2 300 μL, pH 6.5), the photocatalytic activity of as-prepared

MNFSs was much higher than that of nano- and micron-sized α-Fe_2O_3. The reaction rate of MNFSs was more than twice that of nano-sized α-Fe_2O_3 and nearly 12 times faster than that of the micron-sized α-Fe_2O_3. MNFSs could control the slow-release of ·OH and thus improve the utilization efficiency of ·OH, due to the high specific surface area together with the special porous structure. Magnetic measurement showed that MNFSs exhibited magnetic properties at room temperature. Thus it could be collected after use for magnetic separation during the environmental remediation. The MNFSs were reused several times without any appreciable reduction in photocatalytic efficiency. These results indicated that MNFSs had potential applications in visible-light photocatalysis for environmental remediation.

References

1 M. R. Hoffmann, S. T. Martin, W. Y. Choi and D. W. Bahnemann, *Chem. Rev.*, 1995, **95**, 69.
2 X. W. Duan, G. Z. Wang, H. Q. Wang, Y. Q. Wang, C. Shen and W. P. Cai, *CrystEngComm*, 2010, **12**, 2821.
3 C. Burda, X. B. Chen, R. Narayanan and M. A. El-Sayed, *Chem. Rev.*, 2005, **105**, 1025.
4 J. G. Yu, X. X. Yu, B. B. Huang, X. Y. Zhang and Y. Dai, *Cryst. Growth Des.*, 2009, **9**, 1474.
5 E. Hosono, S. Fujihara, H. Lmai, I. Honma, I. Masaki and H. S. Zhou, *ACS Nano*, 2007, **1**, 273.
6 J. G. Yu and X. X. Yu, *Environ. Sci. Technol.*, 2008, **42**, 4902.
7 H. Zhang and Y. F. Zhu, *J. Phys. Chem. C*, 2010, **114**, 5822.
8 L. Li, M. Krissanasaeranee, S. W. Pattinson, M. Stefik, U. Wiesner, U. Steiner and D. Eder, *Chem. Commun.*, 2010, **46**, 7620.
9 Z. B. Lei, W. S. You, M. Y. Liu, G. H. Zhou, T. Takata, M. Hara, K. Domen and C. Li, *Chem. Commun.*, 2003, (17), 2142.
10 J. Wu, F. Duan, Y. Zheng and Y. Xie, *J. Phys. Chem. C*, 2007, **111**, 12866.
11 R. Van de Krol, Y. Q. Liang and J. Schoonman, *J. Mater. Chem.*, 2008, **18**, 2311.
12 B. Sun, J. Horvat, H. S. Kim, W. S. Kim, J. Ahn and G. X. Wang, *J. Phys. Chem. C*, 2010, **114**, 18753.
13 L. P. Zhu, H. M. Xiao, X. M. Liu and S. Y. Fu, *J. Mater. Chem.*, 2006, **16**, 1794.
14 H. Dai, R. Z. Zhang, Y. C. Du, L. Zhang, J. G. Deng, Y. S. Xia, Z. X. Zhao, X. Meng and Y. X. Liu, *Inorg. Chem.*, 2011, **50**, 2534.
15 X. W. Lou, L. A. Archer and Z. C. Yang, *Adv. Mater.*, 2008, **20**, 3987.
16 L. C. Jia, W. P. Cai and H. Q. Wang, *J. Mater. Chem.*, 2009, **19**, 7301.
17 J. B. Wiley, F. Li, J. B. He and W. L. Zhou, *J. Am. Chem. Soc.*, 2003, **125**, 16166.
18 F. Jiao, A. Harrison, J. C. Jumas, A. V. Chadwick, W. Kockelmann and P. G. Bruce, *J. Am. Chem. Soc.*, 2006, **128**, 5468.
19 L. Z. Wang, F. Q. Tang, K. Ozawa, Z. G. Chen, A. Mukherj, Y. C. Zhu, J. Zou, H. M. Cheng and G. Q. Lu, *Angew. Chem., Int. Ed.*, 2009, **48**, 7048.
20 S. H. Xuan, L. Y. Hao, W. Q. Jiang, L. Song, Y. Hu, Z. Y. Chen, L. F. Fei and T. W. Li, *Cryst. Growth Des.*, 2007, **7**, 430.
21 X. J. Liu, H. Wang, C. H. Su, P. W. Zhang and J. B. Bai, *J. Colloid Interface Sci.*, 2010, **351**, 427.
22 Y. Z. Li, H. Xie, S. F. Jin, J. J. Han and X. J. Zhao, *J. Phys. Chem. C*, 2010, **114**, 9706.
23 H. Wang, H. L. Wang and W. F. Jiang, *Chemosphere*, 2009, **75**, 1105.

9712 | *J. Mater. Chem.*, 2012, **22**, 9704–9713

This journal is © The Royal Society of Chemistry 2012

24 H. G. Yang, G. Liu, S. Z. Qiao, C. H. Sun, Y. G. Jin, S. C. Smith, J. Zou, H. M. Cheng and G. Q. Lu, *J. Am. Chem. Soc.*, 2009, **131**, 4078.
25 W. Luo, L. H. Zhu, N. Wang, H. Q. Tang, M. J. Cao and Y. B. She, *Environ. Sci. Technol.*, 2010, **44**, 1786.
26 K. S. W. Sing, D. H. Everett, R. A. W. Haul, L. Moscou, R. A. Pierotti, J. Rouquerol and T. Siemieniewska, *Pure Appl. Chem.*, 1985, **57**, 603.
27 S. Y. Zeng, K. B. Tang, T. W. Li, Z. H. Liang, D. Wang, Y. K. Wang and W. W. Zhou, *J. Phys. Chem. C*, 2007, **111**, 10217.
28 L. P. Zhu, H. M. Xiao and S. Y. Fu, *Cryst. Growth Des.*, 2007, **7**, 177.
29 J. H. Ye, J. W. Tang and Z. G. Zou, *Angew. Chem., Int. Ed.*, 2004, **43**, 4463.
30 X. Y. Hu, T. Zhang, Z. Jin, S. Z. Huang, M. Fang, Y. C. Wu and L. Zhang, *Cryst. Growth Des.*, 2009, **9**, 2324.
31 F. Ji, C. L. Li, J. H. Zhang and L. Deng, *Desalination*, 2011, **269**, 284.
32 M. A. Oturan, E. Brillas and I. Sires, *Chem. Rev.*, 2009, **109**, 6570.
33 M. T. Suidan, D. D. Dionysiou, E. Bekou, I. Baudin and J. M. Laine, *Appl. Catal., B*, 2000, **26**, 153.
34 L. Rideh, A. Wehrer, D. Ronze and A. Zoulalian, *Ind. Eng. Chem. Res.*, 1997, **36**, 4712.
35 J. Gimenez, D. Curco and M. A. Queral, *Catal. Today*, 1999, **54**, 229.
36 G. A. Parks, *Chem. Rev.*, 1965, **65**, 177.
37 W. Z. Tang and C. P. Huang, *Environ. Technol.*, 1996, **17**, 1371.
38 S. Zhang, X. Zhao, H. Niu, Y. Shi, Y. Cai and G. Jiang, *J. Hazard. Mater.*, 2009, **167**, 560.
39 S. M. Kim and A. Vogelpohl, *Chem. Eng. Technol.*, 1998, **21**, 187.
40 H. Q. Wang, G. H. Li, L. C. Jia, G. Z. Wang and C. J. Tang, *J. Phys. Chem. C*, 2008, **112**, 11738.
41 M. Valko, M. Izakovic, M. Mazur, C. J. Rhodes and J. Telser, *Mol. Cell. Biochem.*, 2004, **266**, 37.
42 S. Shamaila, A. K. L. Sajjad, F. Chen and J. L. Zhang, *Appl. Catal., B*, 2010, **94**, 272.
43 K. Rajeshwar, Y. Ming and C. R. Chenthamarakshan, *J. Photochem. Photobiol., A*, 2002, **147**, 199.
44 R. Amal, V. N. H. Nguyen and D. Beydoun, *Chem. Eng. Sci.*, 2003, **58**, 4429.
45 G. Tian, Y. Chen, W. Zhou, K. Pan, C. Tian, X. R. Huang and H. Fu, *CrystEngComm*, 2011, **13**, 2994.
46 H. X. Li, Z. F. Bian, J. Zhu, D. Q. Zhang, G. S. Li, Y. N. Huo, H. Li and Y. F. Lu, *J. Am. Chem. Soc.*, 2007, **129**, 8406.